

Materials Advances

Volume 4
Number 10
21 May 2023
Pages 2237-2394

rsc.li/materials-advances



ISSN 2633-5409

PAPER

Kartik Sau, Shin-ichi Orimo *et al.*

The role of cation size in the ordered-disordered phase transition temperature and cation hopping mechanism based on $\text{LiCB}_{11}\text{H}_{12}$

Cite this: *Mater. Adv.*, 2023,
4, 2269

The role of cation size in the ordered–disordered phase transition temperature and cation hopping mechanism based on $\text{LiCB}_{11}\text{H}_{12}^{\ddagger}$

Kartik Sau, *^{ab} Shigeyuki Takagi, ^c Tamio Ikeshoji, ^b Kazuaki Kisu, ^c
Ryuhei Sato ^a and Shin-ichi Orimo *^{ac}

Complex hydrides are of great interest for being potential candidates for the solid electrolyte of all-solid-state batteries owing to their exceptionally high ionic conductivity at high temperatures. Hereafter, we study a model system ($\text{LiCB}_{11}\text{H}_{12}$) using molecular dynamics (MD) simulations based on a reported force field to investigate the role of cation size in the ordered–disordered phase-transition temperature (T_{tran}) and cationic diffusion. The MD results indicate that the lowering of T_{tran} is due to the high cell volume (by introducing a large-size cation) that eases the anionic rotation. The results are further confirmed by performing a few additional MD simulations by keeping a fixed cation size while varying cell volumes. In addition, the study provides insights into the cationic density distribution, the bottlenecks of the cationic path, and its hopping mechanism with increasing cationic sizes. These findings are of fundamental importance for achieving a lower transition temperature and higher cationic diffusion for practical applications.

Received 29th September 2022,
Accepted 21st March 2023

DOI: 10.1039/d2ma00936f

rsc.li/materials-advances

1. Introduction

Batteries have been playing a significant role in meeting the skyrocketing demand for electronic devices and fully electric vehicles. However, the current battery technology based on conventional Li-ion batteries does not satisfy the consumers' needs.^{1–6} All-solid-state batteries (ASSBs), being safer than liquid- or polymer electrolyte-based batteries and having a higher energy density and longer life cycles, are a possible alternative. In the last couple of decades, significant progress has been made in the development of ASSBs⁷ largely based on Li^+ ion conduction,^{8–14} where high ionic conductivity is one of the inevitable prerequisites for electrodes and electrolytes. The most popular electrolytes in ASSBs are $\text{Li}_{10}\text{GeP}_2\text{S}_{12}$ (LISICON-like),¹⁵ $\text{Li}_6\text{PS}_5\text{Br}$ (argyrodite),^{16,17} complex metal-hydrides ($\text{M}_x\text{M}'_y\text{H}_z$, where M can be replaced with alkali or alkaline-earth atoms, and $\text{M}'_y\text{H}_z$ can be replaced with anions: BH_4^- ,^{18,19}

$\text{B}_6\text{H}_6^{2-}$, $\text{B}_{10}\text{H}_{10}^{2-}$, $\text{CB}_9\text{H}_{10}^-$, $\text{B}_{12}\text{H}_{12}^{2-}$, and $\text{CB}_{11}\text{H}_{12}^-$),²⁰ $\text{Li}_{6.55}\text{La}_3\text{Zr}_2\text{Ga}_{0.15}\text{O}_{12}$ (garnet),^{21,22} $\text{Li}_{1.2}\text{Al}_{0.2}\text{Ti}_{1.8}(\text{PO}_4)_3$ (Na superionic conductor or NASICON-type),²³ and $\text{Li}_{0.34}\text{La}_{0.51}\text{TiO}_{2.4}$ (perovskites),^{24,25} in which the ionic conductivity is comparable with current liquid electrolytes.

Among the mentioned classes of materials, complex metal hydrides have recently attracted attention²⁶ owing to their exceptional high cationic conductivity, low density, low toxicity, and soft mechanical properties.²⁷ The anions in this type of materials are identified at body-centered, face-centered (Fig. 1) or hexagonal-close-packed positions, whereas Li^+ ions are found at the interstitial positions of anions. The shapes of the anions are large-quasispherical ($\text{CB}_{11}\text{H}_{12}$ or $\text{CB}_{11}\text{H}_{12}^-$) or ellipsoidal cage-like ($\text{B}_{10}\text{H}_{10}$ or CB_9H_{10}). At a low temperature, the structure, often called an ordered structure, is well defined and symmetric (Fig. 1(a)), whereas at a high temperature, the anions are in the disordered state exhibiting high rotation, and atomic coordinates (C, B, and H) of an anion are not well defined (Fig. 1(b)). Despite high rotation of the anions in the disordered state, their average center of mass is remained fixed at their individual equilibrium sites. The system exhibits a sharp cation-conductive transition above the ordered–disordered phase-transition temperature (T_{tran}), associated with high anionic rotation.^{28–35} The anionic rotational disorder typically generates several cationic sub-lattices for facile cationic diffusion,³⁶ as anionic rotation flattens the potential energy landscape for cation translational motions.^{37–40} However, these sublattice structures are usually accessible for

^a Advanced Institute for Materials Research (WPI-AIMR), Tohoku University, Aoba-ku, Sendai 980-8577, Japan. E-mail: kartik.sau@gmail.com, shin-ichi.orimo.a6@tohoku.ac.jp

^b Mathematics for Advanced Materials Open Innovation Laboratory (MathAM-OIL), National Institute of Advanced Industrial Science and Technology (AIST), c/o Advanced Institute for Materials Research (WPI-AIMR), Tohoku University, Sendai 980-8577, Japan

^c Institute for Materials Research (IMR), Tohoku University, Sendai 980-8577, Japan

† Electronic supplementary information (ESI) available. See DOI: <https://doi.org/10.1039/d2ma00936f>





Fig. 1 (a) Ball-and-stick model of low-temperature ordered LiCB₁₁H₁₂ (the occupancy of Li, C, B, and H at each site is 1.0 with a smaller unit cell size),⁵⁷ whereas (b) shows the high-temperature disordered structure (anion center remains ordered) with site occupancy less than unity and high anionic rotation is indicated by an arrow. In this case, the bigger unit cell size indicated the volume expansion because of the high-temperature. The *a*- and *c*-axes are also shown, and black lines indicate the unit cell. (c) A tetrahedral (Tt) void formed by four anions and an octahedral (Oc) void formed by six anions are shown. The anions are also surrounded by six such Oc sites or voids. Several cation sizes are indicated using different opacities. The corner-shared triangular faces of Oc or Tt are the geometrical bottleneck along the cationic path. The geometrical bottleneck radius is also marked by dotted circles. The red, brown, green, and blue balls represent Li, C, B, and H, respectively, for all cases.

smaller cations (Li⁺, Na⁺, and Ag⁺), as reported in the recent studies.^{4,29–34,41–43} In addition, the ordered–disordered transition occurs at elevated temperatures, which makes this material unfavorable for practical use.

To overcome the mentioned issue, several strategies have been implemented to achieve a lower T_{tran} , such as

1. Using monovalent ions (CB₁₁H₁₂^{−40,44} or CB₉H₁₀[−]) instead of a divalent anion (B₁₂H₁₂^{2−}) that also enhances the cationic vacancies in the system enabling higher cationic diffusion;
2. Alloying two different types of *closo*-borane^{45,46} improves the space inside the structure for easing anionic rotation.

Furthermore, substituting larger alkali-metal cations, such as K⁺, can result in similar favorable ordered–disordered structural transitions at reasonably low temperatures, although K⁺ ion conductivity is reasonably low.⁴⁷ A similar phenomenon was identified in the case of molten salts (CsCl shows a lower melting point than NaCl or KCl).⁴⁸ Despite several experimental studies, the fundamental understanding of hydrides is still vastly speculative; thus, a thorough theoretical simulation study is required to guide the synthesis of a suitable material with a lower T_{tran} and higher cationic conductivity. Inspired by recently reported work on KCB₁₁H₁₂ by Dimitrievska *et al.*,⁴⁷ we conducted molecular dynamics (MD) simulations by systematically varying the cation sizes (essentially by tuning the reported force-field), which was impossible in the first principles-based MD simulation or through experiments. MD simulation has emerged as one of the first growth techniques for understanding the atomistic mechanisms at the atomic level⁴⁹ while avoiding the gap between theory and experiment. Silver iodide,^{50,51} β -alumina,⁵² and Na_{1+x}Zr₂-Si_xP_{3-x}O₁₂ (NASICON) (0 ≤ *x* ≤ 3)⁵³ and a variety of oxides^{54,55} are examples of this successful technique. However, the results of MD simulation strongly depend on how good the inter-atomic potential is. Recently, we developed an interatomic potential parameters model for complex metal hydrides^{44,56} to perform

MD studies that represented ordered–disordered phase transition behavior for Li₂B₁₂H₁₂ and LiCB₁₁H₁₂ as reported in the experiments, and provided several structural insights and information on the hopping mechanism of cationic diffusion for LiCB₁₁H₁₂ which are experimentally challenging to report due to high anionic rotation above T_{tran} .⁵⁷

In this study, we gained further insights into the relationships between cation size and T_{tran} , and cationic hopping mechanisms using predefined force-field-based MD simulations while using the low-temperature structure of LiCB₁₁H₁₂⁵⁷ (Fig. 1(a)). The existing bottleneck radius along the cationic conduction path (Fig. 1(c)) also plays a major role in cationic conduction, which was vastly studied in the other materials (NASICON^{58,59} and Li₁₀GeP₂S₁₂⁶⁰), and remains an untouched area in complex hydrides, which shall be thoroughly studied in this paper. Herein, we used the same structure as LiCB₁₁H₁₂ and systematically varied the cation sizes to avoid the complex role of anionic arrangements (different types of structures are identified for the Na and K counterparts,⁴⁷ where a different anion arrangement also plays a specific role).

II. Methodology

A. Inter-atomic potential

To conduct MD simulations, we used, as previously reported, a combination of Buckingham, harmonic bond, and angle-type potentials:⁴⁴

$$U(r, \theta) = U_{\text{Coulomb+Buckingham}}(r) + U_{\text{bond}}(r) + U_{\text{angle}}(\theta) \quad (1a)$$

$$U_{\text{Coulomb+Buckingham}}(r) = \frac{q_i q_j}{4\pi\epsilon_0 r} + A_{ij} \exp(-r/\rho) - \frac{C_{ij}}{r^6} \quad (1b)$$

$$U_{\text{bond}}(r) = \frac{1}{2} k_r (r - r_0)^2 \quad (1c)$$



$$U_{\text{angle}}(\theta) = \frac{1}{2}k_{\theta}(\theta - \theta_0)^2 \quad (1d)$$

where q_i denotes the charge on the i th ion; A_{ij} and C_{ij} are the short-range overlapped repulsive energy and dispersion energy of atom pairs, respectively; and ρ determines the depth of the potential. r_0 , and θ_0 are the equilibrium bond distance and angle with spring constant k_r , and k_{θ} , respectively. ϵ_0 is the permittivity in the free space.

B. Computational details

Using the previously reported parameters listed in Table 1, we conducted a series of isothermal-isobaric (NPT) MD simulations in the temperature range of 325–525 K with 12 K (some cases 25 K) intervals, and zero atmospheric pressure. The NPT -MD method,⁶¹ which allows changing the simulation box sizes while keeping the angles fixed, was employed. The temperatures and pressure within the system were controlled using thermostatting and barostatting techniques, where some dynamic variables are coupled with particle velocity and simulation box dimensions. We chose the default parameters for the Nose-Hoover thermostatting (100 times of time step) and barostatting (1000 times of time step), as mentioned in the LAMMPS software package.⁶² In the thermostatting case, essentially, a fictitious particle transfers heat from a heat bath to the system, and the parameters indicated in the NPT -MD is equivalent to its mass, although the unit of measurement is not mass. By adjusting this parameter, we can control the particle's inertia. If the value is too small or too large, it may lead to higher temperature fluctuations. This is similar to the barostatting case. It should be noted that the simulations commenced from the reported low-temperature ordered-phase X-ray diffraction structures⁵⁷ for the $\text{LiCB}_{11}\text{H}_{12}$ -system.

Herein, we tuned the Li-H repulsive parameters to mimic different sizes of the cation, where three different sets of parameters were used for the three different sizes of cations (small, medium, and large), as presented in Table S1 (in the ESI[†]). The interaction of the M-H (M = small, medium, and large) pair as a function of distances for different interaction parameters are presented in Fig. 2. For the larger cations, the minima were shifted at larger distances mimicking larger cation sizes. The Li-B interaction was not modified, as the

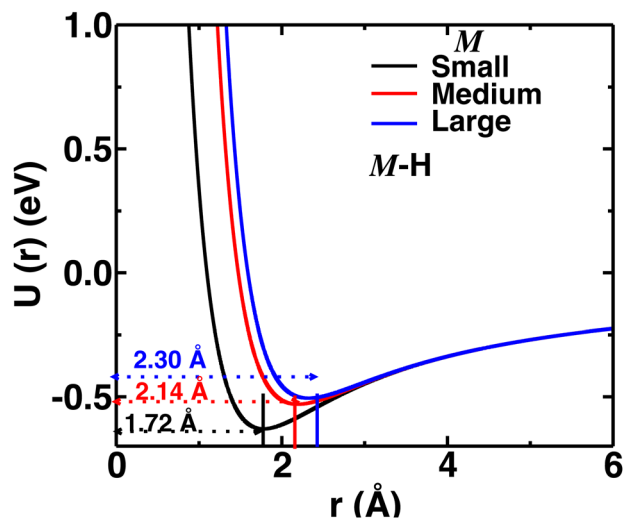


Fig. 2 Pair-wise interaction ($U(r)$ vs. r) for different M-H short-range parameters mimicking small-, medium-, and large-sized cations. The distances of potential minima are also indicated.

cations are usually far from the B atom. Throughout the paper, the three different Li-H interactions are indicated as small-, medium-, and large-sized cations, respectively.

We performed three sets of runs using three different M-H interactions for the previously mentioned temperature range, even though the starting structure for all the simulations was the same as the low-temperature ordered structure reported by Tang *et al.*⁵⁷ for $\text{LiCB}_{11}\text{H}_{12}$. We adopted the above conditions to avoid the complex chemical nature of the different cations. The simulated supercell consisted of $4 \times 4 \times 4$ unit cells comprising 6400 atoms in an orthorhombic symmetry following $Pca2_1$ (no. 29). A time step of 0.5 fs was applied for integration of force using the velocity Verlet algorithm. A typical runtime of 2 ns or longer was used with trajectory samples stored at intervals of 500 fs for detailed analyses, and statistical time averages typically were calculated over the last 1 ns interval. Numerically, to guarantee the thermodynamic convergence properties, a few longer runtime simulations of 10 ns were separately performed. The properties remained the same for a longer time simulation. Periodic boundary conditions in all three directions and the Ewald summation technique for converging long-range Coulomb interactions were applied. A cutoff distance of 13 Å was used for both the short-range interactions and the short-range part of the Ewald summation. A few micro-canonical MD (NVE -MD) simulations were further conducted at 475 K using the final structure obtained from the NPT -MD simulations.

Moreover, we conducted three additional NVE -MD runs at 475 K while keeping Li-H interaction unchanged, same as reported,⁴⁴ for the three different cell volumes, which were respectively selected similar to the cell sizes of the cations (small (V_{Small}), medium (V_{Medium}), and large (V_{Large})). In short, we fixed the cation size and varied the cell volume. Maintaining a constant cation size while varying the cell volume is necessary to comprehend the impact of cell volume on cationic diffusion.

Table 1 Inter-ionic potential parameters employed in this study^a

Species (M)	q_M (e)	A_{M-Li} (eV)	A_{M-B} (eV)	A_{M-H} (eV)	ρ_{M-Li} (Å)	ρ_{M-B} (Å)	ρ_{M-H} (Å)
Li	0.75	0.0	46.08	76.4 ^b	0.4000	0.2853	0.3023
C	0.75	46.08	0.0	0.0	0.2853	0.0	0.2853
B	0.0	80.78	0.0	0.0	0.2853	0.0	0.2853
H	-0.125	76.4	0.0	2175.5	0.3023	0.2853	0.20855

$k_{BB} = 5.375 \text{ \AA}^2 \text{ eV}$, $r_{BBO} = 1.76 \text{ \AA}$ (equilibrium bond length), $k_{CB} = 5.375 \text{ \AA}^2 \text{ eV}$, $r_{CBO} = 1.76 \text{ \AA}$ (equilibrium bond length), $k_{BH} = 9.89 \text{ \AA}^2 \text{ eV}$, $r_{BHO} = 1.2 \text{ \AA}$ (equilibrium bond length), $k_{CH} = 150.5 \text{ \AA}^2 \text{ eV}$, $r_{CHO} = 1.09 \text{ \AA}$ (equilibrium bond length), $k_{BB-H} = k_{B-C-H} = k_{C-B-H} = 0.86 \text{ rad}^2 \text{ eV}$, $\theta_0 = 2.077 \text{ rad}$ (equilibrium angle), and $C_{H-H} = 4.3086 \text{ \AA}^6 \text{ eV}$. ^a The value used from the reported literature.⁴⁴ ^b Different values 46.08, 119.8, and 163.17 are used here for mimicking small, medium, and large cations, respectively.



C. Estimation of key quantities

Cation transport and anionic stability were examined by calculating the mean square displacement (MSD) of both cations and anions following Einstein's relation. The self-diffusion coefficient was calculated from the slope of the MSD for the three-dimensional transport as follows:

$$\text{MSD} = \frac{1}{N} \left\langle \sum_{j=1}^N (\vec{r}_j(t+t') - \vec{r}_j(t))^2 \right\rangle, \quad (2a)$$

$$D = \lim_{t \rightarrow \infty} \frac{\text{MSD}}{6t'}, \quad (2b)$$

where N denotes the total number of mobile atoms in the system, $\vec{r}_j(t)$ is the position vector of the j th ion at time t ; t' is the time difference; and the angular bracket is the average over several points in time. The diffusion coefficient, D , depends on the temperature (T) according to the Arrhenius equation:

$$D = D_0 \exp\left(\frac{-E_a^d}{k_B T}\right), \quad (3)$$

where D_0 denotes the pre-exponential factor, E_a^d represents the activation energy of cationic diffusion, and k_B is the Boltzmann constant.

The anionic reorientational motion is directly identified by calculating the angular autocorrelation function (ζ) of anions:

$$\zeta(t') = \langle \vec{r}(t+t') \cdot \vec{r}(t) \rangle \quad (4)$$

where $\vec{r}(t)$, and $\vec{r}(t+t')$ denote the vector connecting from the center of mass of anions to B, C, or H in the same anion at time t and $t+t'$, respectively. This function typically shows an exponential decay ($\approx e^{-\lambda t'}$) within a short time with a decay rate λ . The anion reorientational activation energy (E_a^r) is calculated using the Arrhenius equation:

$$\lambda = \lambda_0 \exp\left(\frac{-E_a^r}{k_B T}\right) \quad (5)$$

where λ_0 is the pre-exponential factor.

We calculated the "self" part of the van Hove correlation function, $G_S(r, t')$, to understand the cationic hopping mechanism following the formula⁶³

$$G_S(r, t') = \frac{1}{N} \left\langle \sum_{i=1}^N \delta(\vec{r} - (\vec{r}_i(t'+t) - \vec{r}_i(t))) \right\rangle. \quad (6)$$

The potential energy of individual cations is calculated as

$$U_i = \frac{1}{2} \sum_{j=1}^N U_{ij}, \quad (7)$$

where U_{ij} is the interaction potential given in eqn (1a). Finally, free energy (as seen by individual cations), ΔF can be measured from the population density profile, p , relative to another system of cations exhibiting the maximum cation population

density, p_{\max} by the formula:^{44,64–66}

$$\Delta F = -k_B T \ln\left(\frac{p}{p_{\max}}\right). \quad (8)$$

III. Results and discussion

A. Structure and phase transition

We increased the temperature systematically; after a certain level, the anions started rotating around the center of mass, which remained translationally immobile at the crystallographic position (Fig. 1(b)), as reported in our previous study,⁵⁶ where a higher temperature, octahedral (Oc) sites and tetrahedral (Tt) sites were identified, and the surroundings of Oc and Tt-sites are shown in detail in Fig. 1(c). The Oc Li-sites are the center of an octahedron formed by connecting anions, whereas the Tt Li-sites are the center of a tetrahedron formed by connecting anions. Interestingly, all the anion centers are also a center of six octahedral Li-sites. At a high temperature, anionic rotation leads to a high volume change,⁴⁴ as shown in Fig. 3. It exhibits a general trend; the cell volume increases with increasing temperature and shows an abrupt volume change at a particular temperature because of anion rotation, indicating an ordered–disordered phase transition. Another obvious trend is that the cell volume increases with increasing cationic sizes due to the higher cation–anion repulsion. The most interesting result here is the systematic reduction of T_{tran} with increasing cationic sizes, consistent with the previously reported literature, where a systematic lower T_{tran} was identified from Li to K in $\text{ACB}_{11}\text{H}_{12}$ ($A = \text{Li}, \text{Na}, \text{and K}$).⁴⁷ The percentage of volume expansion (δ) at the disordered phase relative to the ordered phase near the



Fig. 3 The time average of cell volume per formula unit (f.u.) (V) as a function of temperature (T) for the $\text{MCB}_{11}\text{H}_{12}$ ($M = \text{small, medium, and large}$) system (325–475 K with an interval 25 K) from the NPT-MD simulation. For comparison, the $V(T)$ for $\text{LiCB}_{11}\text{H}_{12}$ (LCBH) is also shown. The system exhibits a sharp volume change after T_{tran} , whereas the relative volume change with respect to the cell volume in the ordered phase decreases with the increasing cation sizes.



Table 2 A comparison of T_{tran} for several cation sizes in the system $\text{MCB}_{11}\text{H}_{12}$ (M = small, medium, and large)

Cation Size	MD	Expt. ⁴⁷	MD
	T_{tran} (K)	T_{tran} (K)	V change (δ)
Small	425	385 (Li)	12.0
Medium	375	380 (Na)	7.7
Large	350	365 (K)	4.7

$$\delta = \left| \frac{V_t - V_e}{V_t} \right| \%. \quad V_t = \text{cell volume just before the transition point. } V_e = \text{extrapolated cell volume just after the transition point.}$$

transition point also reduces systematically with increasing cation sizes, as listed in Table 2. The difference in transition temperature from experimental and MD simulations could be possibly because of the different M–H interaction potential parameters compared to real Li, Na, and K-systems, *i.e.*, the small system does not correspond to the Li-system. Our primary focus is to capture the transition temperature qualitative trend by varying cation sizes. Since the larger size cation introduces extra inter-anion space,⁴⁷ it offers higher freedom to the anion. In other words, smaller δ generates higher disorder in the system, which lifts the system to the disordered phase. It is also worth noting that a too-large simulation cell (a too-small δ) leads to an unstable system, which was observed in the MD simulation, while we accommodated an even larger sized cation.

The MSD of both cations and anions plays an important role in understanding the transport properties of cations and the structural stability of anions with varying cation sizes, respectively. The MSD of the anion (not distinguishing B or C atoms), and its center of mass were calculated at the upper-temperature end (475 K) (Fig. 4), which saturates quickly because of high anionic rotation; the saturation value is close to the half square diameter of the anion (distance of B or H to the center of mass

of *closo*-borane), indicating indirectly a full rotational mobility and translational immobility of anions. The evidence of direct rotational mobility will be discussed in the next paragraph by calculating the angular auto-correlation function using eqn (4), whereas the immobility of anions is further confirmed by showing a low MSD value of the center of mass of anions and its saturation (Fig. 4(b)). Despite the high rotational mobility, the anions are stable at their crystallographically reported face-centered position for the different cation sizes. It is important to note that the MSD values of the center of mass (CM-MSD) of anions systematically increase with the increasing cation size (Fig. 4(b)). Essentially, the larger CM-MSD value implies a larger fluctuation in CM-anions that could increase the effective anionic radius. The influence of an effective increase in anionic radius will be discussed in the next section.

B. Anionic rotation and cationic diffusion

To quantify the rate of anionic rotation after the T_{tran} , we calculated the anionic angular autocorrelation function, ζ , using eqn (4). Theoretically, after the ordered–disordered transition, the function ζ decays exponentially within a short period, and the decay rate, λ , presented in Fig. 5, as a function of $1000/T$ follows an Arrhenius behavior. The activation energies of anionic reorientation, E_a^r , for different cation sizes were calculated from the fitted straight line using eqn (5), where the E_a^r remains almost the same (0.12, 0.15, and 0.13 eV for small-, medium-, and large-sized cations, respectively) in agreement with the previous reports.^{40,47} Although, the E_a^r does not show any systematic trend, the decay rates, λ , do. In contrast, a systematically lower λ of anions is identified from small to large-sized cation cases. The possible reason could be because of the λ_0 .

Typically the systems (*closo*-boro hydrides or other classes of superionic conductors^{67,68}), where there is no direct connectivity among the anions, cationic diffusion was found to be strongly



Fig. 4 (a) A gross mean square displacement (MSD) of C and B atoms against time difference, t' , in $\text{MCB}_{11}\text{H}_{12}$ (M = small, medium, and large) based on the NVE-MD simulations at 475 K. The MSD value is saturated at a value of $\sim \frac{d^2}{2}$, where d denotes the diameter of anions. The different saturation value is due to the different amounts of the center of mass fluctuation of the anion. (b) MSD of the center of mass of the anion at 475 K for different cation sizes. These results demonstrate that the anions are rotationally mobile (a) and translationally immobile (b).





Fig. 5 Anionic reorientational decay rate λ as a function of $1000/T$ for the $\text{MCB}_{11}\text{H}_{12}$ (M = small, medium, and large) system (325–550 K with an interval of 25 K). The continuous line lines are fitted from the data points after the transition, and activation energies of anion reorientation are calculated from the slope of the fitted line following eqn (3). The dotted lines indicate just connecting the data points below the ordered–disordered temperatures.

associated with the anionic reorientational motion after the ordered–disordered transition, as reported in previous studies.^{37,42,44,56,57,65,69} The activation energy of the cationic diffusion, E_a^d , was calculated from the diffusion coefficient, D (the slope of the MSD in the diffusive region after the transition), for several temperatures according to eqn (3). The plot of the logarithm of D versus the inverse temperature ($1000/T$) is presented in Fig. 6, from where E_a^d can be calculated using the



Fig. 6 Arrhenius plot of the cationic diffusion coefficient for several temperature ranges ($\ln(D)$ vs. $1000/T$) of the $\text{MCB}_{11}\text{H}_{12}$ (M = small, medium, and large) system (325–550 K with an interval of 25 K). The data points below T_{tran} are shown in dotted lines, where diffusivity is significantly low including large statistical errors. The straight lines (continuous) are fitted from the data points and activation energies are calculated from the slope of the straight line following eqn (3).

slope of the straight line from the high-temperature phase. It is worth noting that the differences in diffusion coefficient between the low and high conducting phases are significant, spanning two to three orders of magnitude. We also observed that this difference tends to decrease as cationic sizes increase. This is expected, as larger cationic sizes result in a larger cell volume, facilitating higher cationic diffusion. The activation energies (E_a^d) after the phase transition are found to be 0.17 ± 0.02 , 0.23 ± 0.05 , and 0.29 ± 0.08 eV for small-, medium-, and large-sized cations, respectively, which follows a systematic trend unlike the case for E_a^r . A larger statistical error in the E_a^d value for larger cation cases originates from the diffusion coefficient calculated in a lower temperature range compared to the small-sized cation, as depicted in Fig. 6. Until now, it is quite clear that two factors worked together for the cationic diffusion:

1. The higher anionic reorientational rate, λ , favored a facile cationic diffusion.
2. In contrast, the larger cationic size hindered facile cationic diffusion.

Herein, the larger cation size dominates over the higher anionic reorientational rate, resulting in a relatively higher E_a^d or lower cationic diffusion, as presented in Fig. 6, following the reported trend for $\text{ACB}_{11}\text{H}_{12}$ -systems (where $A = \text{Li}, \text{Na}, \text{and K}$).⁴⁷ Furthermore, a larger fluctuation of CM of anions for larger-sized cations (Fig. 4(b)) could effectively increase the anionic radius, offering a narrower corridor for the lower cationic diffusion. Therefore, we conclude that the lower cationic diffusion for the systematically increasing cationic sizes is reasonable. Consequently, the present MD simulation successfully represents several trends such as T_{tran} , anionic rotational, and cationic diffusion for different cation sizes in accordance with the reported experimental results.

Additionally, anionic rotation and its valuable insights are investigated in this paragraph, as this information is not yet studied in detail. We calculated the anionic angular autocorrelation functions separately for C (ζ_C) in an anion and compared them with the angular auto-correlation of anion, ζ_{CB11} , (not distinguishing C or B), as displayed in Fig. 7. Interestingly, the ζ_C shows a slower decay than ζ_{CB11} . This behavior is identified for all the cation size cases (Fig. 7, in which we only compare for the large-sized cations), whereas the ζ_C systematically follows the same trend as the gross anionic reorientational rate. The slower decay of ζ_C compared with ζ_{CB11} is mainly due to the higher Coulombic charge of C compared with B (Table S1 in the ESI[†]). The high charge on C leads to a stronger interaction with the surroundings (mostly the cations), which is against the faster C rotational motion.

C. Atomistic mechanisms and cationic path

Atomistic insights are the origins of different macroscopic behaviors with increasing cationic sizes and the factors that are responsible for fast cationic motion. A three-dimensional isosurface population density was calculated for cations along with H, as presented in Fig. 8(a), (b), and (b) for the small-, medium-, and large-sized cations, respectively. The cationic density pattern demonstrates a significant difference





Fig. 7 Angular autocorrelation function $\zeta(t')$ of the C and anion from NVE-MD simulation at 475 K for $\text{MCB}_{11}\text{H}_{12}$ ($M = \text{small, medium, and large}$) system. CB_{11} means that the averaging is performed over twelve atoms (one C and eleven B atoms), whereas C indicates the averaging over only C. The function $\zeta(t')$ of the anion (CB_{11}) for a large-sized cation system is also included for the comparison.

with increasing cation sizes. There are two high-density sites; one is surrounded by four anions, which is favorable for the small-size cation, whereas the other less-preferred high-density sites are surrounded by six anions. The site preference changes from small to large-sized cation cases. To understand the high-density site location with high precision, we performed X-ray diffraction (XRD) pattern calculation by placing the atoms at the highest population density locations for small-, and large-sized cation cases (Fig. 9). For comparison, we also included XRD for the Tt- and Oc-sites, and both the peaks (MD sites and crystallographic Oc- and Tt-sites) are consistent, which reconfirms that the high-density sites' areas are Oc-, and Tt-sites.

Most importantly, there is a transition from the Tt-site occupancy to the Oc-site occupancy with increasing cation sizes, which was also speculated in the previous report.⁴⁷

To understand the reason behind the switching of the transition in occupancy, the energy of individual cations was calculated using eqn (7) and merged them in a single unit cell, then we counted the potential energy and number of particle in a three-dimensional grid. Finally, we calculated the average energy by dividing the total count in each grid (averaging was also done over the number of frames) and represented it in a three-dimensional isosurface plot (Fig. 10). For small-sized cations, the Tt-sites are energetically favorable because of the stronger Coulombic attraction of cations at the Tt-site and monovalent anions (Fig. 10(a)). While cation size increased the short-range repulsion between cations occupying the Tt-sites and anions is stronger, as the anion to Tt-site distance is shorter ($\approx 4.15 \text{ \AA}$) than the anion to Oc-site distance ($\approx 4.79 \text{ \AA}$). Thus, the stronger short-range repulsion for the large-sized cations dominates over the Coulombic attraction, as displayed in the potential energy landscape (potential energy isovalue for small-, medium-, and large-sized cation cases were -1.70 , -1.79 , -1.85 eV , respectively). It modifies the potential energy landscape significantly for the cation movement and the Tt-site becomes energetically less favorable. However, the Oc-sites, which are slightly far from the anion center facing lower repulsion, are found to be energetically favorable, as identified in the energy profile in Fig. 10(b) and (c). The above scenario is demonstrated graphically using a schematic diagram of free energy variation (following eqn (8)) along with the potential energy while increasing cation sizes (represented in the bottom row in Fig. 10).

Therefore, the density pattern and energy landscape clearly indicate different cation hopping mechanisms while increasing cationic sizes. In this context, we calculated the self-part of the van Hove correlation function, $G_s(r, t')$, for two different cation sizes (small, and large) to understand the hopping mechanism



Fig. 8 Isosurface density plots of the cation (isovalues of $2 \times 10^4 \text{ \AA}^{-3}$ (orange) and $6 \times 10^5 \text{ \AA}^{-3}$ (red)) and H-atom for $\text{MCB}_{11}\text{H}_{12}$ ($M = \text{small, medium, and large}$) in a $2 \times 2 \times 2$ supercell obtained using OVITO⁷⁰ software at 475 K from NVE-MD simulations. (a) Isovalue $7.5 \times 10^{-5} \text{ \AA}^{-3}$ (blue) for small-sized cation. (b) Isovalue $7.5 \times 10^{-5} \text{ \AA}^{-3}$ (blue) for medium-sized cation. (c) Isovalue $7.5 \times 10^{-5} \text{ \AA}^{-3}$ (blue) for large-sized cation. Tt- and Oc-sites formed by anions are marked. We choose different H isovalues for different sizes of cation cases for better visualization.





Fig. 9 (a) and (b) X-Ray diffraction pattern comparison from maximum density isosurfaces and experimental (Expt.) crystallographic sites for small-, and large-sized cation cases, respectively. The inset shows the isosurface density and their corresponding maxima (indicated by balls).



Fig. 10 (Top row) Free-energy isosurface plots in purple (calculated using eqn (8)) combined with the potential energy of the cations (yellow) using eqn (7) in a single unit cell. The small-, medium-, and large-sized cation cases are marked by (a), (b), and (c), respectively. The isovalue of 0.07 eV value is used for all three cases, whereas -1.89 , -1.75 , and -1.70 eV are used for potential energy isosurface (yellow) for the small-, medium-, and large-sized cations, respectively. (Bottom row) Schematic representation of two-dimensional free energy distribution from Tt to Oc-sites. The favorable potential energy schematic diagrams are also added using yellow dotted lines.

(Fig. 11). Fig. 11(a) and (b) demonstrate two distinct behaviors: the first peak and second peak for small-sized cations are not well separated, as Oc–Tt distance and Tt–Tt distances are closer (≈ 5 Å) and the number of Tt-sites two times more enabling faster cationic diffusion. Thus, the hopping mechanism for the

small-sized cation case is Tt to Tt *via* meta-stable Oc sites, as is already reflected in Fig. 8, whereas there is a distinct second peak in the case of a large-sized cation, which is at a distance near 7 Å (the Oc to Oc site distance is 6.77 Å), and thus the hopping mechanism is Oc to Oc *via* meta-stable Tt-sites.





Fig. 11 (a) The self-van Hove correlation function, $G_s(r, t')$, as a function of radial distance (r) and time (t') for $MCB_{11}H_{12}$ (M = small, medium, and large) at 475 K from the NVE-MD simulations for two different cation sizes ((a) indicates small-sized, whereas (b) indicates large-sized), shown on a logarithmic scale for better visualization.

Therefore, the different type of cation hopping behavior is reconfirmed by analyzing $G_s(r, t')$.

The bottleneck radius along the cationic path plays an important role in determining the cationic path at the high conducting phase, which is one of the untouched areas in this material. As there are many H-atoms in this system, it is complicated to define the bottleneck with respect to the H. Therefore, the bottlenecks are defined with respect to the anion centers, as shown in Fig. 12 along with the isosurface density plot for the large-sized cation. Interestingly, the cationic path

follows through the center of the triangular bottlenecks, which are the triangular faces of octahedron and tetrahedron formed by the connecting center of anions. The bottleneck radius, the inner circle of the triangle, was calculated for all the cases (small-, medium-, and large-sized cations). The bottleneck radii are 3.9, 4.2, and 4.4 Å for the small-, medium-, and large-sized cations, respectively. The calculated bottleneck radius, in this case, is larger than the reported bottleneck for the other systems (NASICONs⁷¹), which is because of the calculation method; we choose the anion center instead of the H. Interestingly, the bottleneck radius systematically increases with increasing the cationic sizes, as expected, and it is in favor of the high cationic diffusion.⁷¹ However, the incremental effective bottleneck radius may not be big enough for the larger-sized cations, hindering cationic diffusion.

To reconfirm our findings, we further conducted a few MD simulations, keeping the cation size fixed as Li^+ , while varying the cell volumes (detailed in the Section 2). The anionic rotational motion systematically increases with increasing cell volume (Fig. S1 in the ESI[†]), whereas the anionic motion is faster than the rotational motion of individual C (Fig. 13(a)), following a similar rotational trend as reflected for several cation size cases (Fig. 7). The anion CM-MSD also followed a similar trend, *i.e.*, the CM-MSD saturation value systematically increases with increasing cell volume. However, the cationic MSD followed a trend opposite to that of different cationic size cases. The MSD of cations systematically increased with the increasing cell volume, which was expected; a bigger cell size offered a wider corridor (bottleneck) for fast cationic diffusion. We also focussed on how the cation occupancy varies while systematically increasing the cell volumes by displaying isosurface density plots for cations and H (Fig. S2, ESI[†]). Interestingly, the cation density systematically switches from the Oc-site to the Tt-site on increasing the cell sizes. In the case of the smaller cell size, the cations at the Tt-sites and anion are in closer proximity; thus, the stronger short-range repulsion makes the Tt-site less favorable for the cations, while the Oc-sites are more favorable, as they are at a far distance. On the other hand by using a large-sized simulation cell, the short-range repulsion



Fig. 12 A triangular bottleneck (shaded area) is drawn along the cationic path from Oc (yellow) to Tt (cyan) sites and a schematic free energy landscape for two dimensions (red) is also shown to identify the saddle point, which is exactly located at the center of bottleneck radius, marked by a black dotted circle. The isosurface density plot of the large-sized cation with isovalues of $5.0 \times 10^5 \text{ \AA}^{-3}$ (red) in a single unit cell is also included for the understanding of the cationic path. The anion centers (magenta) are also marked along with the Oc and Tt-sites.



due to the dominating short-range repulsion over the Coulombic attraction while increasing the cation size. However, the Tt-sites (two-fold larger than Oc-sites) were in favor of faster cationic diffusion, which was further confirmed by using fixed-size cation with varying cell sizes. Additionally, the smaller percentage of cell volume change resulted in a higher anionic freedom that lifted up the system from an ordered state to a disordered state. Thus, a guideline for superior materials could be keeping a smaller-sized or same-sized cation in a bigger simulation cell, as observed in $\text{MgB}_{12}\text{H}_{12}\cdot 12\text{H}_2\text{O}$.⁷² However, in real materials, the cation sizes and the anionic arrangement play combined roles. Therefore, understanding the role of cation size in ionic conduction and T_{tran} separately is fundamental to optimize these properties.

Data availability

The data that support the findings of this study are available from the corresponding author (K. S.) upon reasonable request.

Author contributions

K. S. and T. I. conceived the study and planned the research. K. S. performed the molecular dynamics simulations and the results were discussed among all the authors. S. T. helped to improve the figures. K. S. wrote the manuscript and all the authors contributed to revisions.

Conflicts of interest

The authors declare no competing financial or non-financial interests.

Acknowledgements

K. S. is thankful for the JSPS International Fellowship. This work was supported by JSPS KAKENHI Grant-in-Aid for Scientific Research on Innovative Areas “Hydrogenomics”, No. JP18H05513 and JSPS Fellowship grant (21F21345). We gratefully acknowledge the Center for Computational Materials Science of Institute for Materials Research, Tohoku University, for permitting the use of MASAMUNE-IMR (MAterial science Supercomputing system for Advanced MULTiscale simulations toward NExt-generation Institute of Material Research) (project no. 202203-SCKXX-0408).

References

- 1 J. Goodenough, H.-P. Hong and J. Kafalas, *Mater. Res. Bull.*, 1976, **11**, 203.
- 2 U. Von Alpen, M. Bell and H. Höfer, *Solid State Ionics*, 1981, **3–4**, 215.
- 3 A. Hooper, *J. Phys. D: Appl. Phys.*, 1977, **10**, 1487.
- 4 T. Udovic, M. Matsuo, A. Unemoto, N. Verdál, V. Stavila, A. Skripov, J. Rush, H. Takamura and S. Orimo, *Chem. Commun.*, 2014, **50**, 3750.
- 5 J. Fergus, *Solid State Ionics*, 2012, **227**, 102.
- 6 A. Lubimtsev, P. Kent, B. Sumpster and P. Ganesh, *J. Mater. Chem. A*, 2013, **1**, 14951.
- 7 T. Famprakis, P. Canepa, J. Dawson, M. Islam and C. Masquelier, *Nat. Mater.*, 2019, **18**, 1278.
- 8 P. Bron, S. Johansson, K. Zick, J. Der Günne, S. Dehnen and B. Roling, *J. Am. Chem. Soc.*, 2013, **135**, 15694.
- 9 N. Kamaya, K. Homma, Y. Yamakawa, M. Hirayama, R. Kanno, M. Yonemura, T. Kamiyama, Y. Kato, S. Hama, K. Kawamoto and A. Mitsui, *Nat. Mater.*, 2011, **10**, 682.
- 10 S. Lee, X.-G. Sun, A. Lubimtsev, X. Gao, P. Ganesh, T. Ward, G. Eres, M. Chisholm, S. Dai and H. Lee, *Nano Lett.*, 2017, **17**, 2229.
- 11 K. Takada, *Acta Mater.*, 2013, **61**, 759.
- 12 G. Sahu, Z. Lin, J. Li, Z. Liu, N. Dudney and C. Liang, *Energy Environ. Sci.*, 2014, **7**, 1053.
- 13 V. Thangadurai, S. Narayanan and D. Pinzaru, *Chem. Soc. Rev.*, 2014, **43**, 4714.
- 14 K. Sau, T. Ikeshoji and S. Roy, *Phys. Chem. Chem. Phys.*, 2020, **22**, 14471.
- 15 N. Kamaya, K. Homma, Y. YamaNawa, M. Hirayama, R. Kanno and M. Yonemura, *Nat. Mater.*, 2011, **10**, 682.
- 16 S. Boulineau, M. Courty, J.-M. Tarascon and V. Viallet, *Solid State Ionics*, 2012, **221**, 1.
- 17 R. Rao and S. Adams, *Phys. Status Solidi A*, 2011, **208**, 1804.
- 18 Z. Lodziana and T. Vegge, *Phys. Rev. Lett.*, 2004, **93**, 145501.
- 19 D. Blanchard, A. Nale, D. Sveinbjörnsson, T. Eggenhuisen, M. Verkuijlen, Suwarno, T. Vegge, A. Kentgens and P. De Jongh, *Adv. Funct. Mater.*, 2015, **25**, 184.
- 20 A. Unemoto, K. Yoshida, T. Ikeshoji and S. Orimo, *Mater. Trans.*, 2016, **57**, 1639.
- 21 C. Bernuy-Lopez, W. Manalastas, J. Lopez Del Amo, A. Aguadero, F. Aguesse and J. Kilner, *Chem. Mater.*, 2014, **26**, 3610.
- 22 V. Thangadurai and W. Weppner, *Adv. Funct. Mater.*, 2005, **15**, 107.
- 23 K. Arbi, M. Hoelzel, A. Kuhn, F. García-Alvarado and J. Sanz, *Inorg. Chem.*, 2013, **52**, 9290.
- 24 Y. Inaguma, C. Liqun, M. Itoh, T. Nakamura, T. Uchida, H. Ikuta and M. Wakihara, *Solid State Commun.*, 1993, **86**, 689.
- 25 V. Thangadurai, A. Shukla and J. Gopalakrishnan, *Chem. Mater.*, 1999, **11**, 835.
- 26 R. Mohtadi and S. Orimo, *Nat. Rev. Mater.*, 2016, **2**(3), 16091.
- 27 A. Unemoto, M. Matsuo and S. Orimo, *Adv. Funct. Mater.*, 2014, **24**, 2267.
- 28 T. J. Udovic, M. Matsuo, A. Unemoto, N. Verdál, V. Stavila, A. V. Skripov, J. J. Rush, H. Takamura and S. Orimo, *Chem. Commun.*, 2014, **50**, 3750.
- 29 T. Udovic, M. Matsuo, W. Tang, H. Wu, V. Stavila, A. Soloninin, R. Skoryunov, O. Babanova, A. Skripov, J. Rush, A. Unemoto, H. Takamura and S. Orimo, *Adv. Mater.*, 2014, **26**, 7622.
- 30 W. Tang, T. Udovic and V. Stavila, *J. Alloys Compd.*, 2015, **645**, S200.
- 31 W. Tang, M. Matsuo, H. Wu, V. Stavila, A. Unemoto, S. Orimo and T. Udovic, *Energy Storage Mater.*, 2016, **4**, 79.



- 32 B. Hansen, M. Paskevicius, M. Jørgensen and T. Jensen, *Chem. Mater.*, 2017, **29**, 3423.
- 33 W. Tang, M. Dimitrievska, V. Stavila, W. Zhou, H. Wu, A. Talin and T. Udovic, *Chem. Mater.*, 2017, **29**, 10496.
- 34 M. Jørgensen, P. Shea, A. Tomich, J. Varley, M. Bercx, S. Lovera, R. Černý, W. Zhou, T. Udovic, V. Lavallo, T. Jensen, B. Wood and V. Stavila, *Chem. Mater.*, 2020, **32**, 1475.
- 35 A. V. Soloninin, M. Dimitrievska, R. V. Skoryunov, O. A. Babanova, A. V. Skripov, W. S. Tang, V. Stavila, S. Orimo and T. J. Udovic, *J. Phys. Chem. C*, 2017, **121**, 1000, DOI: [10.1021/acs.jpcc.6b09113](https://doi.org/10.1021/acs.jpcc.6b09113).
- 36 A. V. Skripov, O. A. Babanova, A. V. Soloninin, V. Stavila, N. Verdal, T. J. Udovic and J. J. Rush, *J. Phys. Chem. C*, 2013, **117**, 25961.
- 37 Z. Lu and F. Ciucci, *J. Mater. Chem. A*, 2016, **4**, 17740.
- 38 J. Varley, K. Kweon, P. Mehta, P. Shea, T. Heo, T. Udovic, V. Stavila and B. Wood, *ACS Energy Lett.*, 2017, **2**, 250.
- 39 K. Kweon, J. Varley, P. Shea, N. Adelstein, P. Mehta, T. Heo, T. Udovic, V. Stavila and B. Wood, *Chem. Mater.*, 2017, **29**, 9142.
- 40 M. Dimitrievska, P. Shea, K. Kweon, M. Bercx, J. Varley, W. Tang, A. Skripov, V. Stavila, T. Udovic and B. Wood, *Adv. Energy Mater.*, 2018, **8**, 1703422.
- 41 M. Paskevicius, M. Pitt, D. Brown, D. Sheppard, S. Chumphongphan and C. Buckley, *Phys. Chem. Chem. Phys.*, 2013, **15**, 15825.
- 42 N. Verdal, J.-H. Her, V. Stavila, A. Soloninin, O. Babanova, A. Skripov, T. Udovic and J. Rush, *J. Solid State Chem.*, 2014, **212**, 81.
- 43 M. Paskevicius, B. Hansen, M. Jørgensen, B. Richter and T. Jensen, *Nat. Commun.*, 2017, **8**, 15136.
- 44 K. Sau, T. Ikeshoji, S. Kim, S. Takagi and S. I. Orimo, *Chem. Mater.*, 2021, **33**, 2357.
- 45 S. Kim, H. Oguchi, N. Toyama, T. Sato, S. Takagi, T. Otomo, D. Arunkumar, N. Kuwata, J. Kawamura and S. Orimo, *Nat. Commun.*, 2019, **10**, 1081.
- 46 S. Kim, K. Kisu, S. Takagi, H. Oguchi and S. Orimo, *ACS Appl. Energy Mater.*, 2020, **3**, 4831.
- 47 M. Dimitrievska, H. Wu, V. Stavila, O. Babanova, R. Skoryunov, A. Soloninin, W. Zhou, B. Trump, M. Andersson, A. Skripov and T. Udovic, *J. Phys. Chem. C*, 2020, **124**, 17992.
- 48 M. Broström, S. Enestam, R. Backman and K. Mäkelä, *Fuel Process. Technol.*, 2013, **105**, 142.
- 49 M. S. Islam and C. A. Fisher, *Chem. Soc. Rev.*, 2014, **43**, 185.
- 50 P. Vashishta and A. Rahman, *Phys. Rev. Lett.*, 1978, **40**, 1337.
- 51 P. Vashishta, R. K. Kalia, J. P. Rino and I. Ebbsjö, *Phys. Rev. B: Condens. Matter Mater. Phys.*, 1990, **41**, 12197.
- 52 J. Walker and C. Catlow, *J. Phys. C: Solid State Phys.*, 1982, **15**, 6151.
- 53 P. P. Kumar and S. Yashonath, *J. Phys. Chem. B*, 2002, **106**, 7081.
- 54 L. Malavasi, C. A. Fisher and M. S. Islam, *Chem. Soc. Rev.*, 2010, **39**, 4370.
- 55 E. Kendrick, J. Kendrick, K. S. Knight, M. S. Islam and P. R. Slater, *Nat. Mater.*, 2007, **6**, 871.
- 56 K. Sau, T. Ikeshoji, S. Kim, S. Takagi, K. Akagi and S. Orimo, *Phys. Rev. Mater.*, 2019, **3**, 075402.
- 57 W. Tang, A. Unemoto, W. Zhou, V. Stavila, M. Matsuo, H. Wu, S. Orimo and T. Udovic, *Energy Environ. Sci.*, 2015, **8**, 3637.
- 58 D. T. Qui, J. Capponi, J. Joubert and R. Shannon, *J. Solid State Chem.*, 1981, **39**, 219.
- 59 H. Kohler and H. Schulz, *Mater. Res. Bull.*, 1985, **20**, 1461.
- 60 T. Krauskopf, S. P. Culver and W. G. Zeier, *Chem. Mater.*, 2018, **30**, 1791.
- 61 M. Parrinello and A. Rahman, *J. Appl. Phys.*, 1981, **52**, 7182.
- 62 S. Plimpton, *J. Comput. Phys.*, 1995, **117**, 1.
- 63 P. Hopkins, A. Fortini, A. J. Archer and M. Schmidt, *J. Chem. Phys.*, 2010, **133**, 224505.
- 64 Y. Wang, W. D. Richards, S. P. Ong, L. J. Miara, J. C. Kim, Y. Mo and G. Ceder, *Nat. Mater.*, 2015, **1**, 1026.
- 65 K. Sau and T. Ikeshoji, *J. Phys. Chem. C*, 2020, **124**, 20671.
- 66 P. Padma Kumar and S. Yashonath, *J. Phys. Chem. B*, 2002, **106**, 7081.
- 67 K. Sau, T. Ikeshoji, S. Takagi, S. Orimo, D. Errandonea, D. Chu and C. Cazorla, Colossal Barocaloric Effects in the Complex Hydride $\text{Li}_2\text{B}_{12}\text{H}_{12}$, *Sci. Rep.*, 2021, **11**, 11915.
- 68 T. Famprikis, J. Dawson, F. Fauth, O. Clemens, E. Suard, B. Fleutot, M. Courty, J.-N. Chotard, M. Islam and C. Masquelier, *ACS Mater. Lett.*, 2019, **1**, 641.
- 69 W. Tang, M. Matsuo, H. Wu, V. Stavila, W. Zhou, A. Talin, A. Soloninin, R. Skoryunov, O. Babanova, A. Skripov, A. Unemoto, S. Orimo and T. Udovic, *Adv. Energy Mater.*, 2016, **6**, 1502237.
- 70 A. Stukowski, *Modell. Simul. Mater. Sci. Eng.*, 2009, **18**, 015012.
- 71 K. Pramanik, K. Sau and P. P. Kumar, *J. Phys. Chem. C*, 2020, **124**, 4001.
- 72 K. Kisu, A. Dorai, S. Kim, R. Hamada, A. Kumatani, Y. Horiguchi, R. Sato, K. Sau, S. Takagi and S. Orimo, *J. Mater. Chem. A*, 2022, **10**, 24877.
- 73 A. Skripov, R. Skoryunov, A. Soloninin, O. Babanova, W. Tang, V. Stavila and T. Udovic, *J. Phys. Chem. C*, 2015, **119**, 26912.

